



TECHNICAL ARTICLE

Measurement and Identified Prediction Equation for Residual Stress Distribution in Aluminum Alloy A5052 under Various Pneumatic Shot Peening Conditions

Takahiro Ohta , Jiaxin He, Shun Takahashi, and Ninshu Ma

Submitted: 7 October 2022 / Revised: 4 January 2023 / Accepted: 29 January 2023 / Published online: 5 April 2023

Pneumatic shot peening with zircon shot of four different diameters was performed on an aluminum alloy. The effects of air pressure, shot diameter, and material on shot velocity were experimentally investigated based on direct measurement technology using a high-speed camera and a particle image velocimetry. The residual stress distribution through the thickness direction was systematically measured by the x-ray diffraction method and quantitatively evaluated by an identified equation considering the shot velocity, diameter, and materials. This identified equation can quickly and accurately predict the residual stress distribution owing to shot peening with different shot diameters and velocities for industrial applications.

Keywords almen intensity, particle image velocimeter, residual stress, shot diameter, shot peening, shot velocity

1. Introduction

The shot peening process, wherein shots are impacted onto a metal surface at high velocity, improves the fatigue strength by creating a compressive residual stress field around the impacted metal surface. Shot peening is applied to several components of automobiles and aircraft.

The main parameters that affect shot peening include shot diameter, shot velocity, shot material, impact angle, and coverage (Ref 1). Shots of diameter 0.1–1.3 mm are generally used for the process. The conventional shot materials, such as steel, glass, and ceramics are mainly used. Coverage is the ratio of the indentation area caused by the shot to the metal surface area and is usually controlled by peening time and shot mass. To obtain a stable compressive residual stress field, coverage is usually set at 100% or higher. There are two types of shot peening: the impeller type and the pneumatic type. In the pneumatic type, the shot is accelerated by high-pressure air, and

the shot velocity is controlled by the air pressure. In several cases, the deformation (arc height) of a standard steel strip, referred to as an Almen strip, is used to examine the effect of shot peening. The arc height increases with peening time and becomes approximately saturated with time. This saturated arc height, referred to as the Almen intensity, is an index of the effect of shot peening (Ref 1–8). Guagliano (Ref 3) expressed the Almen intensities for varying shot diameter for steel and ceramic shots as a cubic equation for shot velocity. Miao et al. (Ref 4) presented linear regression equations up to the second order of the relationship between Almen intensity, shot velocity, and diameter for steel and ceramic shots. Zinn and Scholtes (Ref 5), Barker et al. (Ref 6), Cao et al. (Ref 7), and Muller and Urffer (Ref 8) have investigated the relationship between the Almen intensity and shot diameter analytically or experimentally; however, few approximate equations were provided.

The effect of the shot peening conditions on the residual stress distribution has been studied through several experiments and numerical simulations. Hills et al. (Ref 9), Al-Hassani (Ref 10), Al-Obaid (Ref 11), Watanabe and Hasegawa (Ref 12), and Ogawa and Asano (Ref 13) investigated the effect of shot velocity and shot diameter on the residual stress distribution by theoretical calculations using the Hertzian stress. Schiffner (Ref 14), Jiang et al. (Ref 15), Lin et al. (Ref 16), Zhao et al. (Ref 17), Tao and Gao (Ref 18), Gallitelli et al. (Ref 19), Li et al. (Ref 20), and Li et al. (Ref 21) used the numerical simulation method to investigate the residual stress distribution by varying the shot diameter and velocity. Wang et al. (Ref 22), Zinn and Scholtes (Ref 5), and Miao et al. (Ref 23) performed shot peening on various materials and experimentally investigated the relationship between the shot velocity and residual stress distribution. The results of the previous studies (Ref 1, 11, 14, 16, 17) on the effect of shot velocity and diameter on the residual stress distribution are shown in Fig. 1(a) and (b), respectively. The depth of the maximum compressive residual stress and the region of compressive stress increase with the

Takahiro Ohta, Department of Mechanical Engineering, Tokai University, 4-1-1 Kitakaname, Hiratsuka, Kanagawa 259-1292, Japan; and Department of Mechanical System Engineering, Hiroshima Institute of Technology, 2-1-1 Miyake, Saeki-ku, Hiroshima 731-5193, Japan; **Jiaxin He**, Course of Mechanical Engineering, Graduate School, Tokai University, 4-1-1 Kitakaname, Hiratsuka, Kanagawa 259-1292, Japan; **Shun Takahashi**, Department of Mechanical System Engineering, Tokai University, 4-1-1 Kitakaname, Hiratsuka, Kanagawa 259-1292, Japan; and **Ninshu Ma**, Joining and Welding Research Institute, Osaka University, 11-1 Mihogaoka, Ibaragi, Osaka 567-0047, Japan. Contact e-mail: t.ohta.62@cc.it-hiroshima.ac.jp.

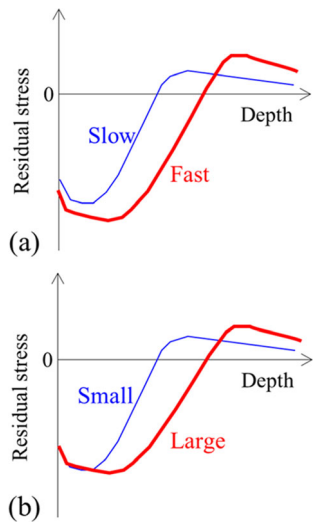


Fig. 1 Schematic diagram of the residual stress distribution after shot peening: (a) effect of shot velocity and (b) effect of shot diameter

increase in shot velocity and diameter. The maximum compressive residual stress difference is insignificant.

However, few studies have formulated the effects of shot diameter, velocity, and material on the compressive residual stress distribution. Al-Hassani (Ref 10) and Al-Obaid (Ref 11) showed the relationship between the depth of plastic strain, the shot velocity, and shot diameter when a material is impacted by a single shot. Watanabe and Hasegawa (Ref 12) employed the calculation method of Al-Obaid (Ref 11) to obtain an equation correlating the depth of plastic strain and the shot velocity and diameter. Ogawa and Asano (Ref 13) presented an equation for the maximum compressive residual stress and its depth correlating the shot velocity, diameter, and density. Wang et al. (Ref 22) presented a relationship between the Almen intensity and the maximum compressive stress, its depth, the region of compressive stress, and the yield stress of the material. Robertson (Ref 24) proposed an approximate expression for the residual stress distribution. Miao et al. (Ref 23) and Gariépy et al. (Ref 25) evaluated the residual stress distribution using the approximate equation proposed by Robertson (Ref 24). Tao and Gao (Ref 18) proposed a method for predicting residual stress distribution by correlating the coefficients of the equation proposed by Robertson (Ref 24) for the shot velocity and diameter, considering a temperature rise. Although this method was a highly accurate prediction method, it had six coefficients because it used linear regression up to the third order. Gallitelli et al. (Ref 19) expressed the surface stress, maximum compressive stress, and depth as a function of shot velocity, diameter, and density. This method employed a complex equation and required the determination of several coefficients. Li et al. (Ref 21) proposed a method to optimize shot velocity, coverage, and distance using the Box–Behnken design response surface methodology for finite element method results. Daoud et al. (Ref 26) used a second-order and artificial neural network model to predict the distribution of residual stresses. Ralph et al. (Ref 27) proposed a method to predict residual stress distribution by machine learning the results of finite element method modeling and experiments.

In the case of pneumatic shot peening, because the shots are small in diameter and move at high velocity through the

chamber, it is difficult to measure the shot velocity, and only a few studies have focused on shot velocity measurement. Zinn and Scholtes (Ref 5) measured the shot velocities of steel shot (S110, S170 and S230) and investigated the relationship between residual stress distribution, Almen intensity and shot velocity. Miao et al. (Ref 23) used a ceramic shot Zirshot Z425 to measure the shot velocity and investigate the effect of shot velocity on Almen intensity and residual stress distribution. Barker et al. (Ref 6) used steel shot (ASR110 and ASR550) to measure the shot velocity and investigate the effect of Almen intensity on shot velocity. Muller and Urffer (Ref 8) measured shot velocities in ceramic, glass, and steel beads and obtained equations correlating shot velocity to air pressure, shot diameter, and density. Teo et al. (Ref 28) measured the velocities of steel shots (ASR70 and ASR230) to investigate the relationship between shot velocity and Almen intensity. Ohta and Ma (Ref 29) and Ohta et al. (Ref 30) used a high-speed camera and particle image velocimetry (PIV) to measure the shot velocity of a steel shot (ASR170) and investigate the effect of shot velocity on Almen intensity and residual stress distribution. Ogawa et al. (Ref 31) measured the shot velocities of cast iron, glass, and ceramic shots with different diameters, air pressure, and density. Nanbu et al. [Ref 32] measured the shot velocity in fine particle shot peening and examined the effect of high-pressure air on the shot velocity. Ohta and Ma (Ref 33) measured the shot velocities of fine particle shots (zircon and steel) and reported the relationship between the shot velocity and residual stress distribution. Lin et al. (Ref 16) used the computational fluid dynamics method to simulate the effect of shot diameter and air pressure on shot velocity. Wang et al. (Ref 34) obtained the relationship between roughness and air pressure by experiment and the relationship between roughness and equivalent shot velocity by simulation. They also proposed a method for determining the relationship between equivalent shot velocity and air pressure. Jian et al. (Ref 15), Lin et al. (Ref 16), and Wang et al. (Ref 34) used the same formula to calculate shot velocity with air pressure, shot diameter, and mass flow rate of the shots. Using this formula for shot velocity, they examined the validity of their simulation results for shot velocity and residual stress distribution.

As described above, many studies have been conducted on the effects of shot velocity and shot diameter on residual stress distribution, either experimentally or by numerical simulation; however, few studies have investigated the effects of shot velocity, diameter, and material on residual stress distribution in pneumatic shot peening using directly measured shot velocities. Furthermore, no studies predicted the profile of residual stress from the surface to the interior of the plate for varying shot velocity and diameter using a simple approximate equation.

The objective of this study is to develop an identified equation for residual stress distribution considering shot velocity, diameter, and material, because residual stress due to shot peening has a significant influence on fatigue strength. The shot velocities of ceramic (zircon) shots were measured in pneumatic shot peening, and the relationship between shot velocity, air pressure, and shot diameter was verified. Residual stress distributions in the thickness direction of shot peened specimens were measured to quantitatively evaluate the effect of shot velocity and diameter under various shot peening conditions. The experimental method for predicting residual stress distribution using shot velocity, and diameter was investigated.

2. Experimental Method

2.1 Specimen and Shots

In this study, zircon shots were tested to investigate the effect of shot material on residual stress distribution. The specifications of the shots used in the experiments are given in Table 1. FZB20, FZB40, and FZB100 zircon beads from the Fuji Manufacturing Co were used; they are composed of 60-70% ZrO₂, 28-33% SiO₂, and 10% Al₂O₃.

N-type Almen strips were used to measure the peening intensity. The thickness of the N-type Almen strip was 1.27-1.32 mm, the width was 19 mm, and the length was 76 mm. The specimen used for residual stress measurement was an aluminum alloy (A5052-H34) with a hardness of 68-70 HV, proof stress of 188 MPa, and tensile strength of 244 MPa. The chemical composition of the specimens is shown in Table 2. A5052-H34 is an aluminum alloy formed using solid solution strengthening of magnesium and work hardening by cold working. This alloy does not undergo transformation due to temperature increase or plastic deformation. The thickness of the specimen was 5 mm, the width was 19 mm, and the length was 75 mm.

2.2 Experimental Set-up and Shot Peening Conditions

A pneumatic suction type sandblasting machine (TR-135SB by IRII Co.) was used for the experiments. The experimental set-up is shown in Fig. 2. The specimen was moved back and forth multiple times at a movement speed of 4.2 mm/s to peen on the entire surface. The peening time was calculated in terms of time per 1 mm (number of movements/movement speed of the specimen). The shot peening was applied on one side of the specimen on the entire surface. No significant deformation occurred that could be measured with an Almen gauge. The nozzle hole diameter was 5 mm. The standoff distance was 100 mm.

The air pressure was 0.2-0.6 MPa; shots could not be projected at 0.1 MPa. Barker et al. (Ref 6), Jian et al. (Ref 15), Lin et al. (Ref 16), Teo et al. (Ref 28), and Wang et al. (Ref 34) reported that the mass flow rate of the shots projected affected the shot velocity. In this study, mass flow rate of the shots projected was not controlled; The shot mass flow rate increased with the increase in air pressure. The shot mass flow rates were 0.081 kg/min at 0.2 MPa, 0.509 kg/min at 0.4 MPa, and 0.644 kg/min at 0.6 MPa for FZB100; 0.080 kg/min at 0.2 MPa, 0.770 kg/min at 0.4 MPa, and 1.126 kg/min at 0.6 MPa for FZB40; 0.391 kg/min at 0.2 MPa, 1.506 kg/min at 0.4 MPa, and 2.569 kg/min at 0.6 MPa for FZB20.

Table 1 Specifications of shots

Material	Shot	Diameter, average	Hardness	Specific gravity
Zircon	FZB20	0.850-0.600 mm (0.73 mm)	650-800 HV	3.85
	FZB40	0.425-0.250 mm (0.34 mm)		
	FZB100	0.180-0.125 mm (0.15 mm)		

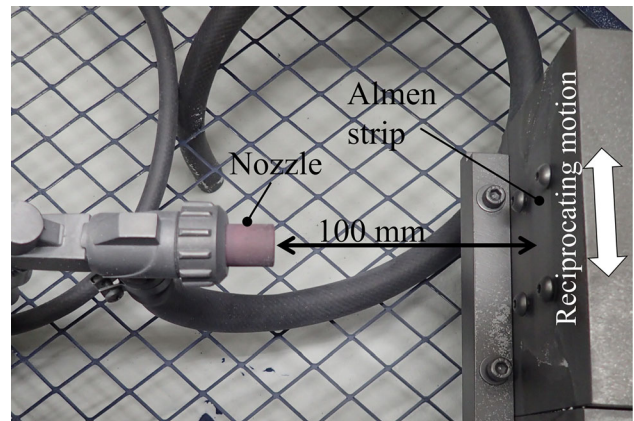


Fig. 2 Experimental set-up

Table 2 Chemical composition, mass% of specimen

Si	Fe	Cu	Mn	Mg	Cr	Zn	Al
0.10	0.31	0.03	0.04	2.5	0.20	0.01	Bal

2.3 Measurement of Shot Velocity

The shot velocity was measured directly using a high-speed camera and PIV. Ohta and Ma (Ref 29, 33) and Ohta et al. (Ref 30) verified the agreement between experimental and simulation results for residual stress distributions with a finite element model using shot velocities measured by the same method. A high-speed camera MEMRECAM ACS-1 from nac Image Technology, Inc. with a shutter speed of 1/250000 s and a frame speed of 1/50000 fps was used. The image resolution was 1028 × 720 pixels, covering an area of approximately 120 mm. The specimen was not set up when the photo was taken because the shot impacting the specimen bounced back, causing complex shot motion and making it difficult to measure the shot velocity.

PIV was performed using an FtrPIV from Flowtec Research Inc. A particle tracking method was used to estimate the movement of shots. The interrogation window was 24 × 24 pixels. In total, 234 pairs of images were analyzed, and the median value was used to determine the shot velocity.

2.4 Measurement of Residual Stress

Residual stress distribution in the aluminum alloy was measured after shot peening by employing the x-ray diffraction method. The portable x-ray residual stress analyzer, μ-X360,

was sourced from Pulstec Co., Ltd. This analyzer uses the $\cos \alpha$ method (Ref 35), which is a established method to measure residual stress in shot peening (Ref 29, 30, 33). The diffraction peak of the (311) plane of aluminum in the Cr $K\alpha$ line was used for the measurement. The x-ray beam was approximately 2 mm in diameter. The incident angle of the x-ray beam was 25° and the diffraction angle was 139.497° . The Young's modulus and Poisson's ratio of the specimens were set to 69.31 GPa and 0.348, respectively.

The residual stress of the specimen was measured on the surface of the specimen after electro-polishing the surface. The electro-polished area was 8 mm in diameter. One specimen was used for each shot peening condition, and residual stresses were measured in two directions at the same depth. If the two stresses differed, additional measurements were taken. The maximum standard deviation of the measured residual stress was 15 MPa. The stress released by electro-polishing was corrected in the measurements by employing a method developed by Moore and Evans (Ref 36). This correction is made using the following equation;

$$\sigma_{r(z_1)} = \sigma_{rm(z_1)} + 2 \int_{z_1}^h \frac{\sigma_{rm(z)}}{z} dz - 6z_1 \int_{z_1}^h \frac{\sigma_{rm(z)}}{z^2} dz$$

where $\sigma_{r(z_1)}$ is the corrected residual stress, z is the distance from the bottom surface, h is the original thickness, z_1 is the distance from the bottom surface to the depth at which the stress is determined after electro-polishing, and $\sigma_{rm(z_1)}$ is the residual stress measured at z_1 .

3. Results and Discussions

3.1 Effect of Air Pressure and Shot Diameter on Shot Velocity

Figure 3(a) and (b) show the images of the in-flight zircon shots FZB20 and FZB100, respectively, captured by the high-speed camera. The air pressure was 0.6 MPa. In both images, the shutter speed was selected to enable a blur-free shoot. FZB100 shots, which had a smaller diameter, were projected in a large number of shots, and the spread of the shot stream was larger than that of FZB20.

Figure 4(a) and (b) show the PIV results at 0.6 MPa for FZB100 and FZB20, respectively. The plots show the shot velocities calculated from 243 pairs of images. The shot velocities varied greatly for each pair at each location due to the scattered distribution of the shots. When there were no shots that could be evaluated within 24×24 pixels, the shot velocity was assumed to be zero. In this study, the median shot velocity calculated from each image was used as a representative of shot velocity at each location.

Figure 5(a) and (b) show the velocity distribution at the nozzle center for FZB100 and FZB20, respectively. The shot velocities of FZB100 rapidly increased after they were projected from the nozzle and reached steady velocities at 120 mm from the nozzle. Moreover, they increased with the increase in air pressure. Inside the nozzle, the high-pressure air can be accelerated to nearly the speed of sound. The shot was accelerated by the air in the nozzle; however, owing to the short length of nozzle, the acceleration was not sufficient, and the shot velocity was lower than the velocity of air when it was projected through the nozzle. Therefore, the shots were

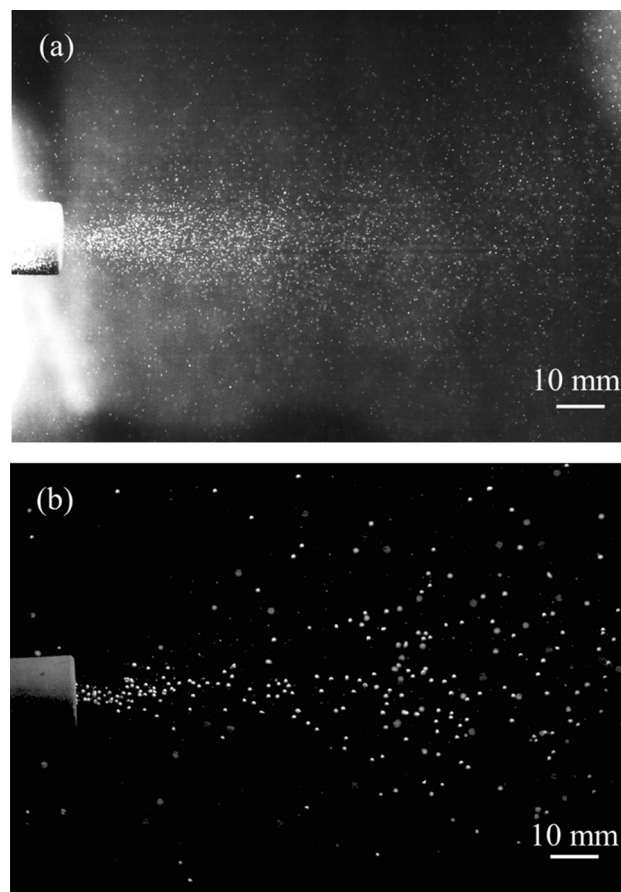


Fig. 3 Images captured by the high-speed camera of the in-flight zircon shots at 0.6 MPa: (a) FZB100 and (b) FZB20

accelerated by high-pressure air after they were projected from the nozzle. The velocity of the air rapidly decreased whereas, the shot flew at a steady velocity, owing to its inertia, because the mass of the shot was larger than that of the air (Ref 16, 29-33). Hence, the shot velocity became higher than the air velocity after a certain distance from the nozzle.

FZB20 showed the same trend as the velocity distribution of the FZB100; however, the shot velocity was lower than that of FZB100. The same trend was observed for tFZB40.

The relationship between the shot velocity, shot diameter, and air pressure was evaluated using the following Eq 1 proposed by Ogawa et al. (Ref 31) and Muller and Urffer (Ref 8).

$$v = a(p - p_o)^b D^c \quad (\text{Eq 1})$$

where v is the shot velocity, p is the air pressure, p_o is the minimum air pressure at which the shot can be projected, D is the average shot diameter, and a , b , and c are coefficients. In this experiment, p_o is 0.1 MPa.

Figure 6 shows the relationship between shot velocity, air pressure, and shot diameter for zircon shots. The plotted data points are the maximum shot velocities obtained via PIV. The plotted lines are the approximate results obtained from Eq 1. The coefficients that minimize the sum of squares of the errors between the experimental and predicted results were determined. The approximations are given in Eq 2 for the zircon shots.

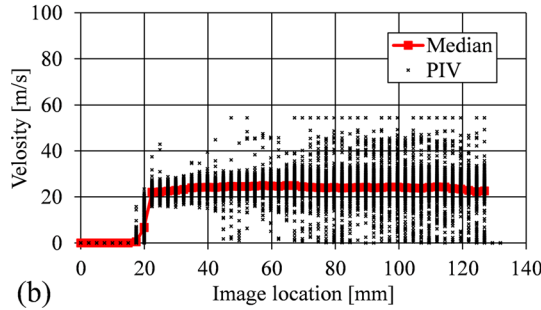
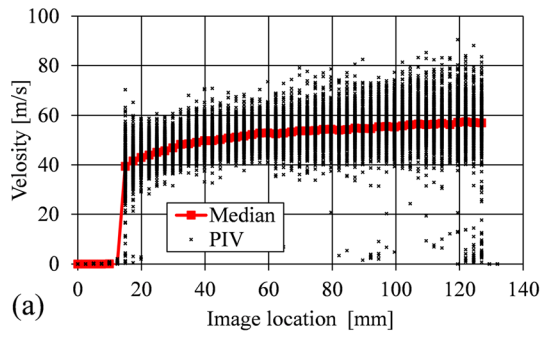


Fig. 4 PIV results for zircon shot at 0.6 MPa at the nozzle center line. The horizontal axis shows the position in the high-speed camera image (Fig. 3) in the shot travel direction. The tip of the nozzle is approximately 20 mm on the horizontal axis: (a) FZB100 and (b) FZB20

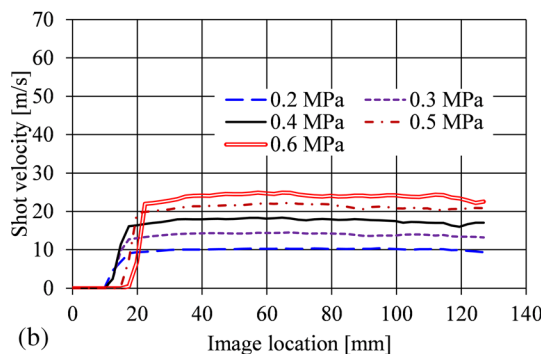
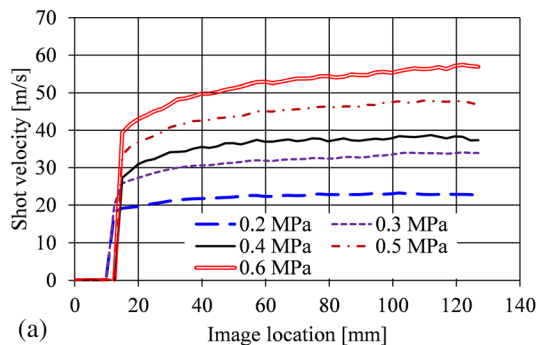


Fig. 5 Shot velocity distribution via PIV at the nozzle center line using zircon shots. The horizontal axis shows the position in the high-speed camera image (Fig. 3) in the shot travel direction: (a) FZB100 and (b) FZB20

$$v = 35.54(p - 0.1)^{0.567} D^{-0.457} \quad (\text{Eq 2})$$

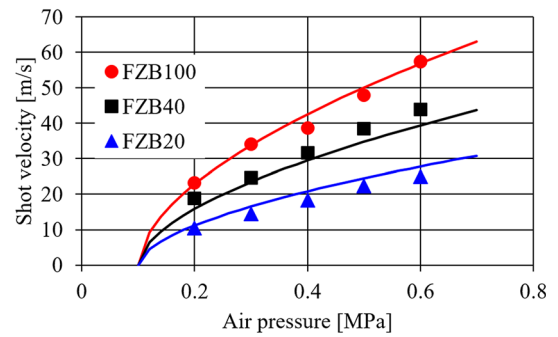


Fig. 6 Effect of air pressure and shot diameter on shot velocity. Plotted experimental data are fitted with lines calculated using Eq 2

The shot velocity was proportional to the air pressure ($p - 0.1$) raised to the power of 0.567. Because the shot velocity decreased as the shot diameter increased, the approximate shot velocities were proportional to approximately -0.457 power of the shot diameters.

3.2 Effect of Shot Velocity and Diameter on the Almen Intensity

The variation of arc height was investigated using *N*-type Almen strips. The saturation curves of the zircon shots (FZB100 and FZB20) are shown in Fig. 7(a) and (b), respectively. The plotted data points are the experimental results and the lines are the values approximated using the following Eq 3, proposed by Kirk (Ref 2);

$$h = \alpha \{1 - \exp(-\beta t^\gamma)\} \quad (\text{Eq 3})$$

where h is the arc height, t is the peening time, and α , β , and γ are coefficients. The coefficients were set to the values that minimize the sum of squares of the errors with the experimental results at each air pressure. The higher the air pressure, the higher is the arc height. The arc height of FZB20, which has a larger shot diameter, was larger than that of FZB100 at the same air pressure. The arc height increased with peening time, and saturated at 4 s/mm in all cases. The saturation time was defined as the time when the rate of change of arc height became less than 10% when the time was doubled in the curve approximated by Eq 3. This trend was the same for FZB40. In this study, the arc height at the saturated peening time of 8 s/mm was evaluated as the Almen intensity.

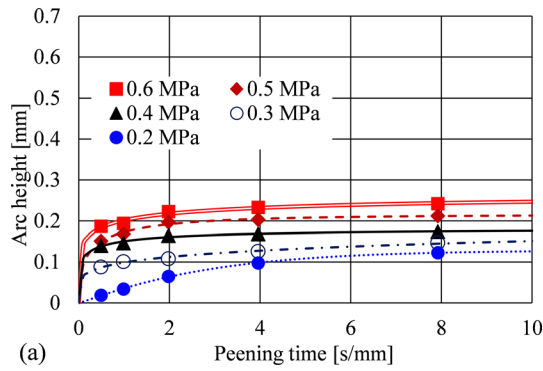
In this study, an equation, similar to the forms of Eq 1 based on the equation proposed by Muller and Urffer (Ref 8), is proposed to express the effect of shot velocity and shot diameter on the Almen intensity as

$$I = kv^n D^m \quad (\text{Eq 4})$$

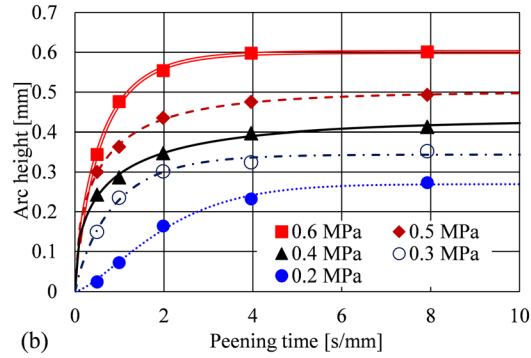
where I is the Almen intensity, v is the shot velocity, D is average shot diameter, and k , n , and m are coefficients. The coefficient k for shot materials includes the effects of specific gravity, Young's modulus, and yield stress. The approximation is shown in Eq 5. The shot velocity was calculated from Eq 2.

$$I = 0.0302v^{1.032} D^{1.084} \quad (\text{Eq 5})$$

The effects of shot velocity and diameter on the Almen intensity are shown in Fig. 8. The data points and lines plotted



(a)



(b)

Fig. 7 Saturation curve of *N*-type Almen strip using zircon shots. The experimental results are plotted, with curves calculated using Eq 3: (a) FZB100 and (b) FZB20

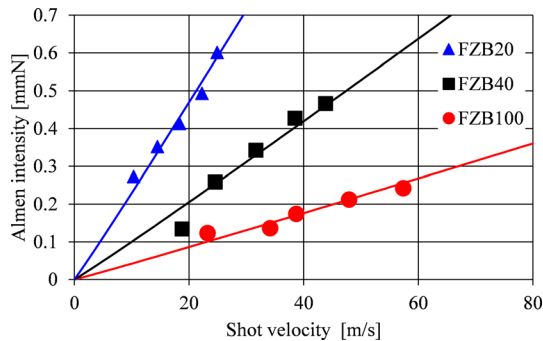


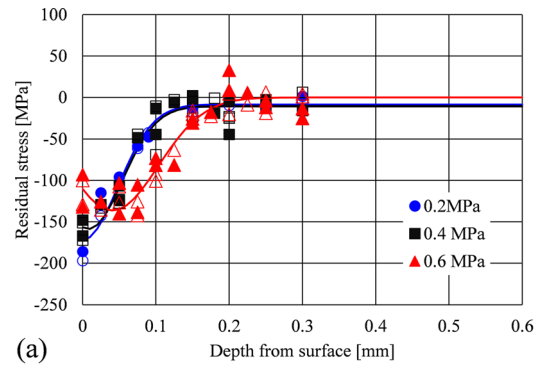
Fig. 8 Effect of shot velocity and diameter on the Almen intensity. Plotted experimental data are fitted with lines calculated using Eq 5

in the figure show the experimental and approximation results, respectively.

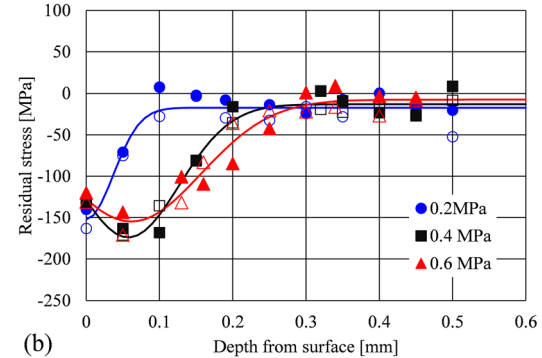
The Almen intensity was approximately proportional to the shot velocity ($v - v_0$). The results of our experiments are consistent with the results in the previous studies, which showed that when the shot velocity was less than 60 m/s, the Almen intensity was approximately proportional to the shot velocity (Ref 3, 5, 7, 30). The Almen intensity was approximately proportional to the shot diameter.

3.3 Effect of Shot Velocity and Diameter on the Residual Stress Distribution through the Thickness Direction

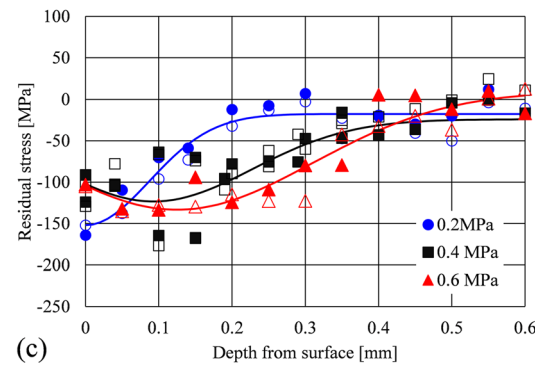
Aluminum alloy (A5052) was shot-peened at air pressures of 0.2, 0.4, and 0.6 MPa, and the residual stress distribution was investigated. Figure 9 shows the measurement results of



(a)



(b)



(c)

Fig. 9 Residual stress distributions after shot peening using zircon shots. Experimental data plotted are *x*-stress (solid) and *y*-stress (open) points fitted with lines calculated using Eq 6: (a) FZB100, (b) FZB40, and (c) FZB20

the residual stress distribution after shot peening. Residual stresses were measured in two specimen directions: the longitudinal (*x*-) and width (*y*-) directions. There was no significant difference between the residual stresses in the *x*- and *y*-directions. When the residual stresses were significantly different, for example, at a depth of 0.1 mm in FZB20, two measurements were made at the same depth at different locations.

For any shot, the range of compressive residual stress deepened with the increase in air pressure and shot diameter.

For FZB100, the maximum compressive stress was at the surface at 0.2 and 0.4 MPa, and the residual stress distribution was approximately the same; the maximum compressive residual stress was inside at 0.6 MPa. For both FZB40 and FZB20, the maximum compressive stress was at the surface at 0.2 MPa; the maximum compressive residual stress was inside at 0.6 and 0.4 MPa. The maximum compressive residual stress

was -200 to -150 MPa in both cases, with no significant difference.

Robertson (Ref 24) proposed Eq 6 as an experimental expression for the residual stress distribution after shot peening and applied it to the residual stress distributions in SAE 5 160 steel peened with CS230 (0.7 mm diameter) and CS660 (1.4 mm diameter) shots. This equation was used by Gariépy et al. (Ref 25) for AA2024-T351 peened with ceramic Zirshot Z425 (0.425-0.600 mm diameter), by Miao et al. (Ref 23) for Al2024-T351 peened with ceramic Zirshot Z425, and by Tao and Gao (Ref 18) for A2060-T8 Al-Li alloy peened with CZ210 (0.13 mm diameter) and CZ300 (0.18 mm diameter). Equation (6) is useful for the prediction of the residual stress distribution.

$$\sigma_{(z)} = A \exp \left[\frac{-2(z - Z_d)^2}{W^2} \right] + B \quad (\text{Eq 6})$$

where $\sigma_{(z)}$ is the in-plane residual stress distribution in the depth direction z , $A + B$ is equal to the maximum residual stress, Z_d is the depth of maximum residual stress, and W is the depth at which the residual stress saturates.

The coefficients A , B , Z_d , and W are identified by the least square method using the measured results. For simplicity, Eq 6 is hereafter called the identified prediction equation for residual stress distribution in all cases. Table 3 summarizes A , B , Z_d , and W for each case. Figure 9 shows the residual stress distribution plotted by solid lines predicted by Eq 6 and its comparison with measured data displayed as marks.

Figure 10 shows the near-surface microstructure after shot peening. Shot peening caused indentation on the surface, which became more pronounced at 0.6 MPa. Under the indentation, the microstructure formed by rolling was curved. Local stratification patterns were observed on the surface at 0.6 MPa. In particular, they were observed with FZB20 at 0.6 MPa (Fig. 10f). In the shot peening, significant surface irregularities were formed on the surface. On subsequent impacts, the convex part was bent and penetrated into the material. On further impacts, the formation, and the bending of the convexity was repeated, forming a localized stratification pattern (Ref 30). Because of the large indentation and surface roughness caused by peening with FZB20 at 0.6 MPa, many local stratification patterns were observed.

Figure 11 shows the hardness distribution near the surface after shot peening. The hardness was measured with a micro-Vickers hardness tester under a load of 100 g. The near-surface area was hardened by shot peening. The larger the shot diameter, the deeper was the hardening depth at 0.6 MPa. This

trend is consistent with the residual stress distribution shown in Fig. 9. At 0.2 MPa, the hardened area was not measured for FZB100 and FZB40, and the hardened area was less than 0.05 mm from the surface. When FZB100 and FZB40 were used, the area of compressive residual stress shown in Fig. 9 was less than 0.1 mm, which was consistent with the hardness distributions at 0.2 MPa.

Because the microstructure deformation was observed near the surface and the hardness distribution near the surface is consistent with the residual stress distribution, it can be concluded that the residual stress distribution was generated from the plastic strain distribution introduced by shot peening.

4. Prediction Method for the Residual Stress Distribution through the Thickness Direction

4.1 Predictive Study of the Effect of Shot Velocity and Diameter for Zircon Shot

To investigate the effect of shot velocity and shot diameter on the residual stress distribution, the coefficients A , B , Z_d , and W in Eq 6 were determined. The identified Eq 7 was proposed to express the effects of shot diameter and velocity on the residual stress distribution in a simpler form.

$$\sigma_{(z)} = (K_A v^{N_A} D^{M_A}) \exp \left[\frac{-2\{z - (K_Z v^{N_Z} D^{M_Z})\}^2}{(K_W v^{N_W} D^{M_W})^2} \right] + (K_B v^{N_B} D^{M_B}) \quad (\text{Eq 7})$$

where $K_{(A,B,Z,W)}$, $N_{(A,B,Z,W)}$, and $M_{(A,B,Z,W)}$ are coefficients. These coefficients were determined to minimize the sum of squares of the errors with A , B , Z_d , and W in Table 2, respectively. $K_{(A,B,Z,W)}$, $N_{(A,B,Z,W)}$, and $M_{(A,B,Z,W)}$ for zircon shots are summarized in Table 4.

Figure 12 shows the relationship between the coefficients in Eq 7 and the shot velocity and diameter. The plotted points are the data in Table 3, and the wireframes are the results of regression using Eq 7. The maximum compressive residual stress, $A + B$, was independent of the shot diameter, velocity, and material. The maximum compressive stress was determined by the yield stress of the aluminum alloy. The depth of maximum compressive stress, Z_d , increased with the increase in shot velocity and diameter. The depth of residual stress, W , increased with the increase in shot velocity and diameter.

Figure 13 shows a comparison between the residual stress distributions predicted using Eq 7 and the measured results for

Table 3 Coefficients in Eq 6 for each condition

Shot	Air pressure, MPa	A, MPa	B, MPa	z_d , mm	W , mm
FZB100	0.2	-1.635×10^2	-8.706	0.000	9.584×10^{-2}
	0.4	-1.485×10^2	-1.061×10^1	8.075×10^{-3}	9.182×10^{-2}
	0.6	-1.362×10^2	-1.840×10^1	4.071×10^{-2}	1.248×10^{-1}
FZB40	0.2	-1.350×10^2	-1.730×10^1	0.000	7.319×10^{-2}
	0.4	-1.609×10^2	-1.312×10^1	5.729×10^{-2}	1.399×10^{-1}
	0.6	-1.473×10^2	-7.517	6.145×10^{-2}	1.910×10^{-1}
FZB20	0.2	-1.344×10^2	-1.764×10^1	0.000	1.735×10^{-1}
	0.4	-9.933×10^1	-2.406×10^1	9.318×10^{-2}	2.688×10^{-1}
	0.6	-1.433×10^2	9.962	1.250×10^{-1}	3.699×10^{-1}

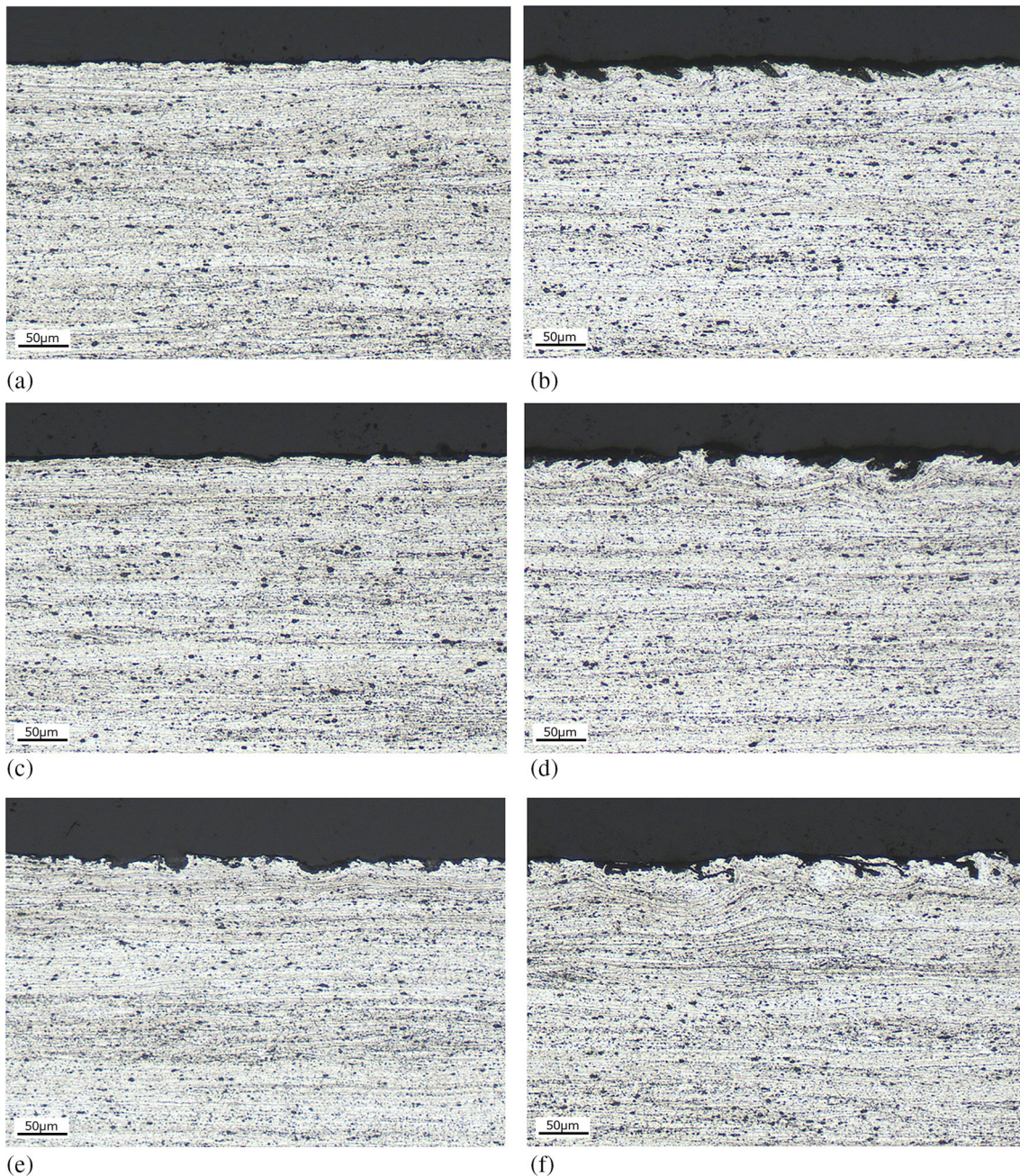


Fig. 10 Microstructure of specimen after shot peening: (a) FZB100 at 0.2 MPa, (b) FZB100 at 0.6 MPa, (c) FZB40 at 0.2 MPa, (d) FZB40 at 0.6 MPa, (e) FZB20 at 0.2 MPa, and (f) FZB20 at 0.6 MPa

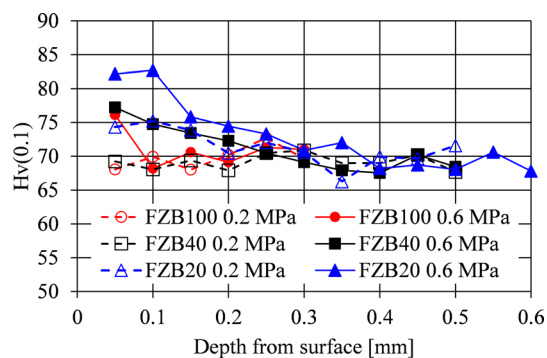


Fig. 11 Hardness distributions near the surface after shot peening

the zircon shots. Because the residual stresses in the x - and y -directions were approximately the same in the experiment, they are plotted with the same points in the figure. In both cases, the measured and predicted results were in good agreement. However, there is a small difference only in the surface stress of FZB100. This prediction method was slightly less accurate for the surface stresses.

Using the proposed simple Eq 7, the residual stress distribution after shot peening at different shot velocities and shot diameters can be predicted. In this study, experiments were conducted in the region of slow shot velocity, and the specimens were only one type of aluminum alloy. In the future, these prediction methods should be verified experimen-

Table 4 Coefficients in Eq 7 for zircon shot

Shot	Coefficients in Eq 8	$K_{(A,B,Z,W)}$	$N_{(A,B,Z,W)}$	$M_{(A,B,Z,W)}$
Zircon, FZB	A , MPa	-1.376×10^2	-3.359×10^{-2}	-1.198×10^{-1}
	B , MPa	-7.732×10^1	-6.503×10^{-1}	-2.968×10^{-12}
	Z_d , mm	1.640×10^{-3}	1.431	1.478
	W , mm	3.078×10^{-2}	8.437×10^{-1}	1.116

tally and numerically over a wider range of shot velocity conditions and with a variety of peened materials.

4.2 Verification using Zircon Shot FZB30

The results in Fig. 13 were obtained by fitting the coefficients of Eq 7 from the experimental results for the residual stress distributions. Therefore, to validate Eq 7, the residual stress distributions were measured when shot peening was performed using zircon shot FZB30 with different shot diameters. The average diameter of FZB30 was 0.51 mm. The experimental conditions and the residual stress measurement method are described in Sect. 2. The shot velocity of FZB30 was calculated using Eq 2. The shot velocity was 13 m/s at 0.2 MPa, 24 m/s at 0.4 MPa, and 32 m/s at 0.6 MPa.

Figure 14 shows a comparison between the residual stress distributions predicted using Eq 7 and the measured results for the FZB30. The measured results and predictions using Eqs 2 and 7 are in good agreement. Within the range of experimental conditions, the prediction method for residual stress distribution using Eq 7 was verified for shot diameters that were not tested.

4.3 Predictive Study of the Effect of Almen Intensity and Shot Diameter

The case of Almen intensity as a parameter was also studied. The identified Eq 8 is proposed to express the effects of shot diameter and Almen intensity on the residual stress distribution in a simpler form. The method is the same as in Sect. 4.1.

$$\sigma_{(z)} = (K_A I^{N_A} D^{M_A}) \exp \left[\frac{-2\{z - (K_Z I^{N_Z} D^{M_Z})\}^2}{(K_W I^{N_W} D^{M_W})^2} \right] + (K_B I^{N_B} D^{M_B}) \tag{Eq 8}$$

where I is the Almen intensity shown in Fig. 8. These coefficients, $K_{(A, B, Z, W)}$, $N_{(A, B, Z, W)}$, and $M_{(A, B, Z, W)}$ were determined to minimize the sum of squares of the errors with A , B , Z_d , and W in Table 3, respectively. The coefficients are summarized in Table 5.

Figure 15 shows the measured results and the results predicted using Eq 8 for the residual stresses. Almen intensities were obtained from the experimental results shown in Fig. 8. The measured and predicted results are in good agreement, and the residual stress distribution can be predicted even with the calculations using Almen intensities.

To verify Eqs 2, 5, and 8, the residual stress distribution was calculated for the zircon shot FZB30, which was not used in the regression. Figure 16 shows a comparison of the residual stress distribution calculated by Eq 8 with the measured results, according to the Almen intensity of FZB30, calculated using Eqs 2 and 5. Almen intensities were 0.208 mmN at 0.2 MPa, 0.395 mmN at 0.4 MPa, and 0.533 mmN at 0.6 MPa. The measured and predicted results are in good agreement. Within the range of experimental conditions, the method presented in

this study can predict the residual stress distribution using Almen intensity.

The identified equation with Almen intensity can be more practically implemented in factories than the method proposed in Sect. 4.1 using directly measured shot velocities. Moreover, it can be used not only for pneumatic shot peening but also for impeller shot peening.

4.4 Applicability of the Proposed Method

The range of applicability of the proposed method was examined. First, the effect of thickness on residual stress distribution was examined. When plastic strain $\varepsilon_{(z)}^*$ occurs and the surrounding area is completely constrained, the stress $\sigma_{(z)}^*$ in a small region $w dz$ at a depth z from the surface occurs as expressed in Eq 9 (Ref 37, 38).

$$\sigma_{(z)}^* = -\frac{E}{(1 - \nu^2)} \varepsilon_{(z)}^* (1 + \nu) \tag{Eq 9}$$

where h is the plate thickness, w is the plate width, E is Young’s modulus, and ν is Poisson’s ratio. When $\sigma_{(z)}^*$ is generated, the stress $\sigma_{P(z)}$ in Eq 10 is generated to balance the forces through the thickness direction (Ref 37, 38).

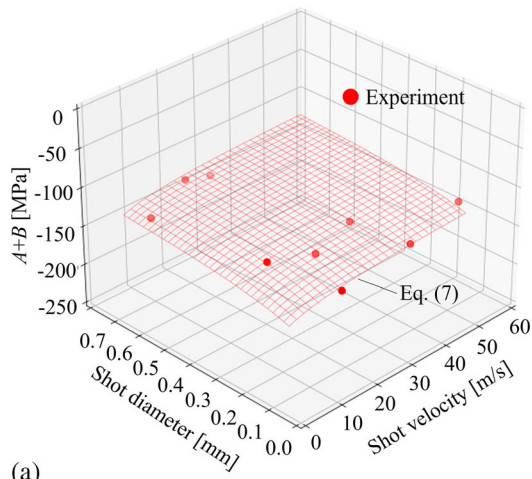
$$\sigma_{P(z)} = \int_0^h \sigma_{(z)}^* w dz / wh \tag{Eq 10}$$

The bending moment M is generated by $\sigma_{(z)}^*$, where M is given by Eq 11. To satisfy the moment equilibrium, the bending stress $\sigma_{M(z)}$ is generated. The final residual stress $\sigma_{R(z)}$ through the thickness direction is the sum of $\sigma_{(z)}^*$, $\sigma_{P(z)}$, and $\sigma_{M(z)}$ (Ref 37, 38).

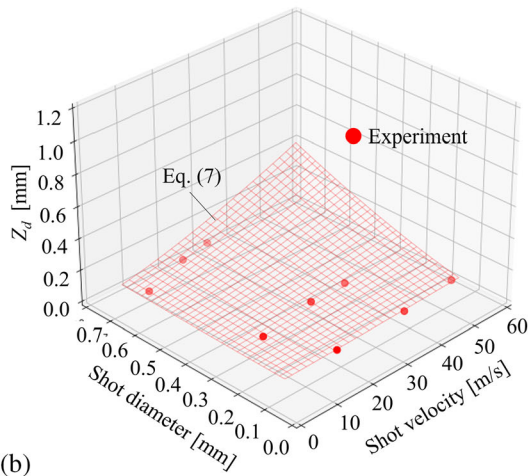
$$M = \int_0^h \sigma_{(z)}^* (z - h/2) w dz \tag{Eq 11}$$

$$\sigma_{R(z)} = \sigma_{(z)}^* + \sigma_{P(z)} + \sigma_{M(z)} \tag{Eq 12}$$

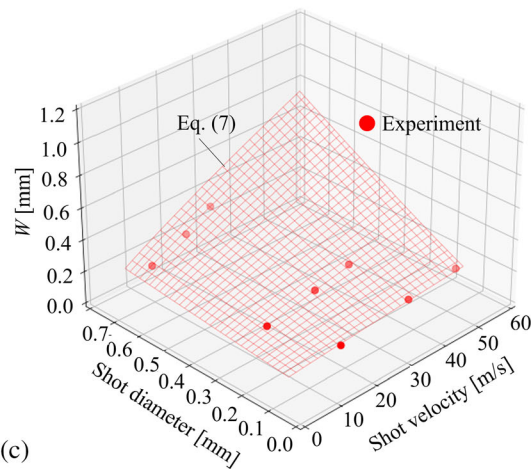
Figure 17 shows the calculated residual stress distribution through the thickness direction when FZB20 shots were used for peening at 0.6 MPa. The plastic strain distribution was set to minimize the sum of squares of the error between the experimental and calculated residual stress. The results of Eq 6 show that the stress was approximately constant at depths greater than 0.6 mm from the surface, whereas the results of Eq 12 show a slight tensile stress, which decreases as the depth increases. Figure 18 shows the effect of thickness on the residual stress distribution. The input plastic strain distribution is the same as in Fig. 17. As the thickness decreased, the influence of bending moments increased, and the stress gradient increased in the region deeper than 0.6 mm from the surface. For thicknesses of 2 and 3 mm, compressive stresses occurred on the back side. The stress distribution in Eq 6 accurately simulated the stress distribution in the vicinity of the surface;



(a)



(b)

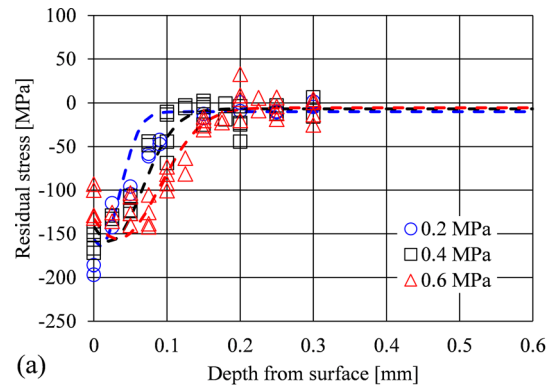


(c)

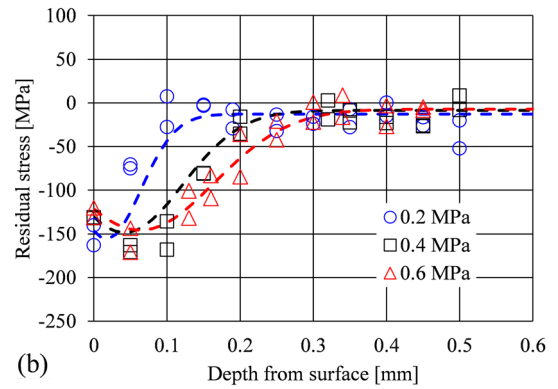
Fig. 12 Relationship between the coefficients in Eq 6 and the shot velocity and diameter. The plots are the data in Table 3, and the wireframes are the results of regression using Eq 7: (a) $A + B$, (b) Z_d , and (c) W

however, the stress distribution in the region not affected by shot peening was not accurate. Equation 6 should not be used to evaluate the stress over the entire thickness, especially for low thicknesses.

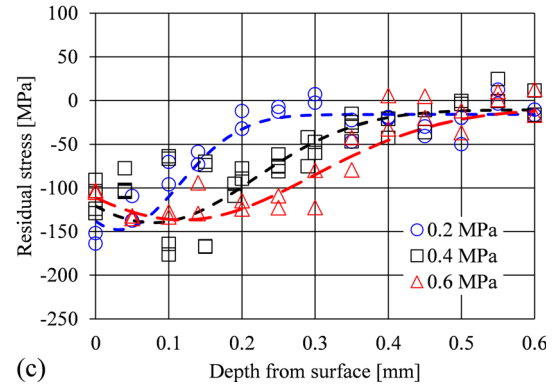
Subsequently, the application of shot peening on high strength materials was examined. Zinn and Scholtes (Ref 5)



(a)



(b)



(c)

Fig. 13 Plotted experimental data are fitted with lines calculated using Eq 7: (a) FZB100, (b) FZB40, and (c) FZB20

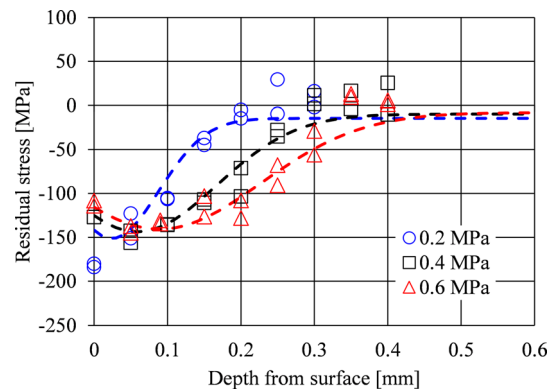


Fig. 14 Verification of the residual stress distribution for FZB30. Plotted experimental data are fitted with lines calculated using Eq 2 and 7

Table 5 Coefficients of Eq 8 for zircon shot

Shot	Coefficients in Eq 8	$K_{(A,B,Z,W)}$	$N_{(A,B,Z,W)}$	$M_{(A,B,Z,W)}$
Zircon, FZB	A , MPa	-1.479×10^2	0.000	-2.286×10^{-2}
	B , MPa	1.401×10^2	4.087	-2.266×10^{-1}
	Z_d , mm	3.234×10^{-1}	1.730	8.712×10^{-2}
	W_s , mm	5.751×10^{-1}	6.499×10^{-1}	3.860×10^{-1}

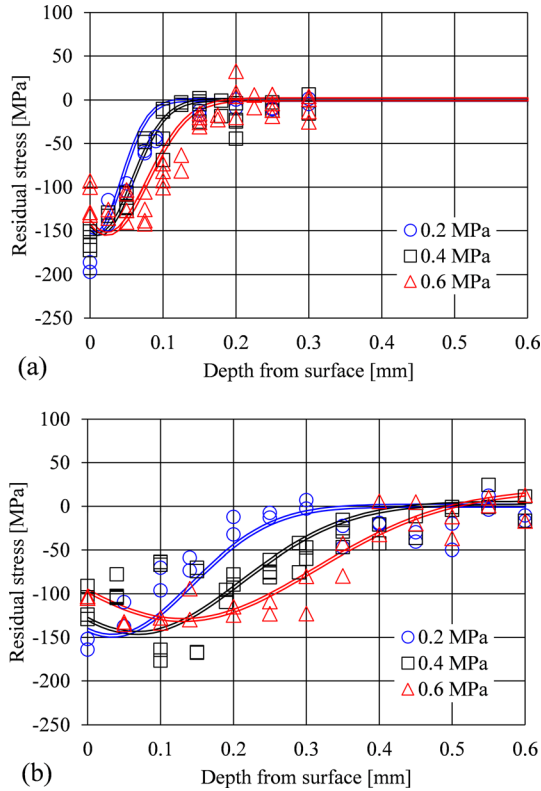


Fig. 15 Plotted experimental data are fitted with lines calculated using Eq 8: (a) FZB100 and (b) FZB20

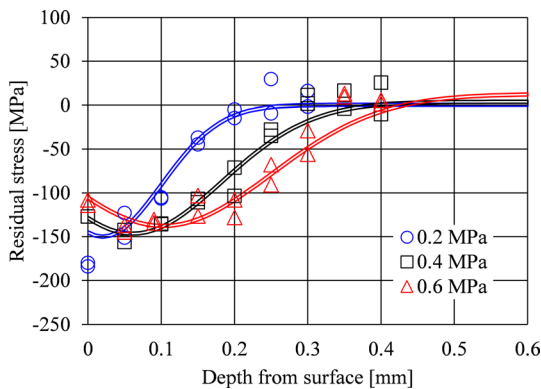


Fig. 16 Verification of the residual stress distribution for FZB30. Plotted experimental data are fitted with lines calculated using Eq 2, 5, and 8

shot peened quenched and tempered chrome-molybdenum-steel (HV500-520) under various conditions and measured the residual stress distribution. They used S110 (average diameter

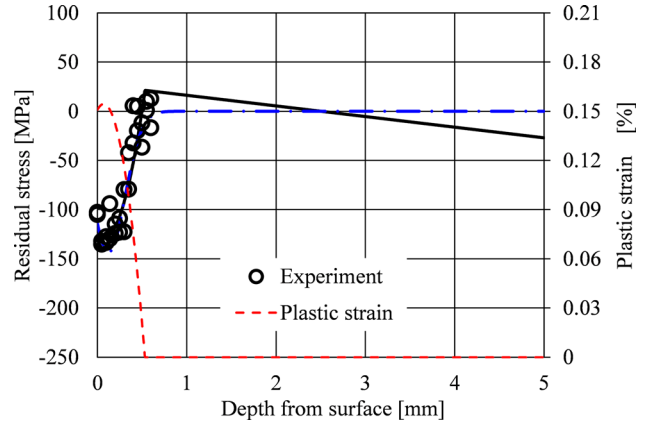


Fig. 17 Calculated residual stress distribution through the thickness direction when FZB20 shots were used for peening at 0.6 MPa. Plotted experimental data are fitted with lines calculated using Eq 12 (solid line) and Eq 8 (dotted-dashed line), and plastic strain is shown as a dotted line

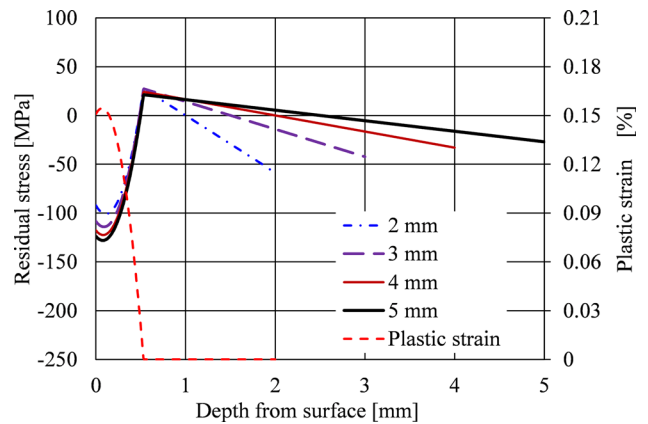


Fig. 18 Calculation results of the effect of thickness on the of residual stress distribution when FZB20 shots were used for peening at 0.6 MPa

0.353 mm), S170 (average diameter 0.500 mm) and S230 shots (average diameter 0.706 mm). A comparison of the residual stress distribution calculated using Eq 8 with the experimental results is shown in Fig. 19. The calculated and experimental results agreed with respect to the trend, however, the difference in stress values was large. In particular, the experimental and calculated results for the S110 at 0.216 mmA and 0.243 mmA differed significantly. Mori et al. (Ref 39) investigated the effect of plastic deformation of the shot on the residual stress and showed that the plastic deformation of the shot did not occur if the flow stress ratio of the shot to the specimen was greater than

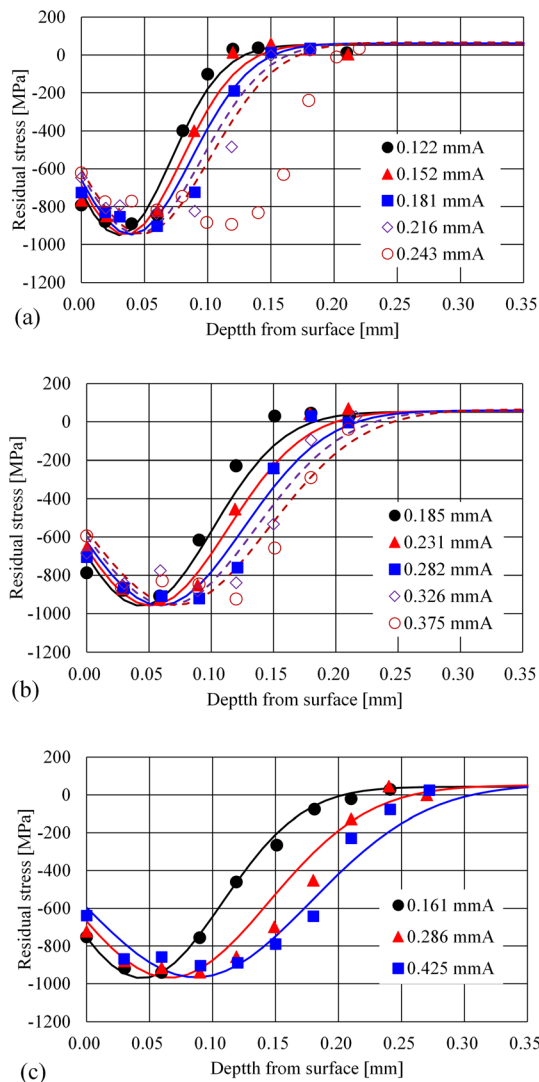


Fig. 19 Comparison of the residual stress distribution calculated by Eq 8 with the experimental results of Zinn and Scholtes (Ref 5): (a) S110, (b) S170, and (c) S230

2. Zinn and Scholtes (Ref 5) did not indicate the hardness of the shot; however, we assumed that the high shot velocity condition caused a large plastic deformation of the shot, which changed the shot peening conditions. When peening conditions varied with shot velocity, for example, when large plastic deformations occur in the shot, it is difficult to predict the residual stress distribution using Eq 8.

The identified equation for the effects of shot diameter and velocity or Almen intensity on the residual stress proposed in this study can be used only in the following cases: (1) when only the residual stress near the peened surface is to be evaluated, and (2) when the shot is sufficiently hard compared to the specimen, such that the shot is not plastically deformed.

5. Conclusion

An identified prediction equation for residual stress distribution through the thickness direction of an aluminum alloy A5052 plate was developed considering the effects of shot

velocity, diameter, and materials. The following detailed conclusions were drawn from the study:

- (1) Shot velocities were directly measured by PIV from images captured by a high-speed camera. The effect of air pressure and shot diameter on shot velocity was expressed by a developed equation for zircon shots. In zircon shot, shot velocity is proportional to the approximately 0.567 power of air pressure and the -0.457 power of shot diameter.
- (2) The quantitatively corresponding equation between residual stress distribution through the thickness direction and shot velocity, and diameter was developed for zircon shots. The coefficients of this equation were inversely identified using systematically measured data.
- (3) The residual stress distribution through the thickness direction at various shot velocities and diameters could be predicted in FZB20, FZB40, and FZB100 using the identified prediction equation. The validity of this equation was demonstrated for a new shot peening condition using FZB30.
- (4) The residual stress distribution through the thickness direction at various Almen intensities and diameters could be predicted using a proposed modification to the same equation. The identified equation with Almen intensity can be more practically implemented in factories. Moreover, it can be used not only for pneumatic shot peening but also for impeller shot peening.

Acknowledgments

The present study was supported by JSPS KAKENHI Grant Numbers 20K05158 and the Amada Foundation Grant Numbers AF-2020019-B3. Mr. Susumu Someya of nac Image Technology Inc. provided assistance in the use of the high-speed camera. Mr. Keiichi Omori of Flowtech Research Inc. gave us useful advice on PIV. Mr. Masaki Okada, a graduate student at Tokai University, and Mr. Naoki Kono and Mr. Koki Mizushima, undergraduate students at Tokai University, assisted in the experiments.

References

1. A. Niku-Lari, Overview on the shot peening process, *Advances in Surface Treatments*. A. Niku-Lari Ed., Elsevier, Pergamon, 1987, p 155–170
2. D. Kirk, Computer-based Saturation Curve Analysis, *Shot Peen. Mag.*, 2005, **19**(4), p 16–21.
3. M. Guagliano, Relating Almen Intensity to Residual Stresses Induced by Shot Peening: A Numerical Approach, *J. Mater. Process. Technol.*, 2001, **110**(3), p 277–286. [https://doi.org/10.1016/S0924-0136\(00\)00893-1](https://doi.org/10.1016/S0924-0136(00)00893-1)
4. H.Y. Miao, S. Larose, C. Perron, and M. Lévesque, An Analytical Approach to Relate Shot Peening Parameters to Almen Intensity, *Surf. Coat. Technol.*, 2010, **205**(7), p 2055–2066. <https://doi.org/10.1016/j.surfcoat.2010.08.105>
5. W. Zinn and B. Scholtes, Influence of shot velocity and shot size on Almen intensity and residual stress depth distributions. *Proceeding 9th International Conference on Shot Peening*, (2005), pp. 379–384. <https://www.shotpeener.com/library/pdf/2005113.pdf>
6. B. Barker, K. Young, and L. Pouliot, Particle velocity sensor for improving shot peening process control. *Proceeding 9th International Conference on Shot Peening*, (2005), pp.385–391. <https://www.shotpeener.com/library/pdf/2005114.pdf>

7. W. Cao, F. Fathallah, and L. Castex, Correlation of Almen Arc Height with Residual Stresses in Shot Peening Process, *Mater. Sci. Technol.*, 1995, **11**(9), p 967–973. <https://doi.org/10.1179/mst.1995.11.9.967>
8. P.P. Muller and D. Urffer, Peening with fused ceramic beads. *Proceeding 3rd International Conference on Shot Peening*, (1987), pp.49–54. <https://www.shotpeener.com/library/pdf/1987221.pdf>
9. D.A. Hills, R.B. Waterhouse, and B. Noble, An Analysis of Shot Peening, *J. Strain Anal. Eng. Des.*, 1983, **18**(2), p 95–100. <https://doi.org/10.1243/03093247V182095>
10. S.T.S. Al-Hassani, Mechanical aspects of residual stress development in shot peening. *Proceeding 2nd International Conference on Shot Peening*, (1981), pp.583–602. <https://www.shotpeener.com/library/pdf/1981050.pdf>
11. Y.F. Al-Obaid, A Rudimentary Analysis of Improving Fatigue Life of Metals by Shot-Peening, *J. Appl. Mech. Trans. ASME*, 1990, **57**(2), p 307–312. <https://doi.org/10.1115/1.2891990>
12. Y. Watanabe and N. Hasegawa, Simulation of residual stress distribution on shot peening. *Proceeding 6th International Conference on Shot Peening*, (1996), pp.530–535. <https://www.shotpeener.com/library/pdf/1996037.pdf>
13. K. Ogawa and T. Asano, Theoretical Prediction of Residual Stress Produced by Shot Peening and Experimental Verification for Carburized Steel, *J. Soc. Mater. Sci. Jpn.*, 2000, **49**(3), p 55–62. https://doi.org/10.2472/jsms.49.3.Appendix_55
14. K. Schiffner, Simulation of Residual Stresses by Shot Peening, *Comput. Struct.*, 1999, **72**(1–3), p 329–340. [https://doi.org/10.1016/S0045-7949\(99\)00012-7](https://doi.org/10.1016/S0045-7949(99)00012-7)
15. T. Jian, W. Zhou, J. Tang, X. Zhao, J. Zha, and H. Liu, Constitutive Modelling of AISI 9310 Alloy Steel and Numerical Calculation of Residual Stress after Shot Peening, *Int. J. Impact Eng.*, 2022, **166**, p 104235. <https://doi.org/10.1016/j.ijimpeng.2022.104235>
16. Q. Lin, P. Wei, H. Liu, J. Zhu, C. Zhu, and J. Wu, A CFD-FEM Numerical Study on Shot Peening, *Int. J. Mech. Sci.*, 2022, **223**, p 107259. <https://doi.org/10.1016/j.ijmesci.2022.107259>
17. J. Zhao, J. Tang, W. Zhou, T. Jiang, H. Liu, and B. Xing, Numerical Modeling and Experimental Verification of Residual Stress Distribution Evolution of 12Cr₂Ni₄A Steel Generated by Shot Peening, *Surf. Coat. Technol.*, 2022, **430**, p 127993. <https://doi.org/10.1016/j.surfcoat.2021.127993>
18. X. Tao and Y. Gao, Influences of Thermal Effects on Residual Stress Fields of an Aluminium-Lithium Alloy Induced by Shot Peening, *Int. J. Adv. Manuf. Technol.*, 2021, **2021**(112), p 3105–3116. <https://doi.org/10.1007/s00170-020-06557-3>
19. D. Gallitelli, D. Boyer, M. Gelineau, Y. Colaitis, E. Rouhaud, D. Retraint, R. Kubler, M. Desvignes, and L. Barrallier, Simulation of Shot Peening: From Process Parameters to Residual Stress Fields in a Structure, *Comptes Rendus Méc.*, 2016, **344**(4–5), p 355–374. <https://doi.org/10.1016/j.crme.2016.02.006>
20. K. Li, C. Wang, X. Hu, Y. Zhou, Y. Lai, and C. Wang, DEM-FEM Coupling Simulation of Residual Stresses and Surface Roughness Induced by Shot Peening of TC₄ Titanium Alloy, *Int. J. Adv. Manuf. Technol.*, 2022, **118**(5), p 1469–1483. <https://doi.org/10.1007/s00170-021-07905-7>
21. B. Li, Z. Qin, H. Xue, Z. Sun, and T. Gao, Optimization of Shot Peening Parameters for AA7B50-T7751 using Response Surface Methodology, *Simul. Model Pract. Theory*, 2022, **115**, p 102426. <https://doi.org/10.1016/j.simpat.2021.102426>
22. S. Wang, Y. Li, M. Yao, and R. Wang, Compressive Residual Stress Introduced by Shot Peening, *J. Mater. Process. Technol.*, 1998, **73**(1–3), p 64–73. [https://doi.org/10.1016/S0924-0136\(97\)00213-6](https://doi.org/10.1016/S0924-0136(97)00213-6)
23. H.Y. Miao, D. Demers, S. Larose, C. Perron, and M. Lévesque, Experimental Study of Shot Peening and Stress Peen Forming, *J. Mater. Process. Technol.*, 2010, **210**(15), p 2089–2102. <https://doi.org/10.1016/j.jmatprotec.2010.07.016>
24. G.T. Robertson, The Effect of Shot Size on the Residual Stresses, Resulting from Shot Peening, *Shot Peen. Mag.*, 1997, **11**(3), p 46–47.
25. A. Gariépy, F. Bridier, M. Hoseini, P. Bocher, C. Perron, and M. Lévesque, Experimental and Numerical Investigation of Material Heterogeneity in Shot Peened Aluminum alloy AA2024-T351, *Surf. Coat. Technol.*, 2013, **219**, p 15–30. <https://doi.org/10.1016/j.surfcoat.2012.12.046>
26. M. Daoud, R. Kubler, A. Bemou, P. Osmond, and A. Polette, Prediction of Residual Stress Fields after Shot-peening of TRIP780 Steel with Second-order and Artificial Neural Network Models Based on Multi-impact Finite Element Simulations, *J. Manuf. Process.*, 2021, **72**, p 529–543. <https://doi.org/10.1016/j.jmapro.2021.10.034>
27. B.J. Ralph, K. Hartl, M. Sorger, A. Schwarz-Gsaxner, and M. Stockinger, (2021) Machine Learning Driven Prediction of Residual Stresses for the Shot Peening Process using a Finite Element Based Grey-box Model Approach, *J. Manuf. Mater. Process.*, 2021, **5**(2), p 39. <https://doi.org/10.3390/jmmp5020039>
28. A. Teo, K. Ahluwalia, and A. Aramcharoen, Experimental Investigation of Shot Peening: Correlation of Pressure and Shot Velocity to Almen Intensity, *Int. J. Adv. Manuf. Technol.*, 2020, **106**, p 4859–4868. <https://doi.org/10.1007/s00170-020-04982-y>
29. T. Ohta and N. Ma, Measurement of Shot Velocity using Particle Image Velocimetry and Numerical Analysis of Residual Stress at Two Shot Peening Conditions, *Mech. Eng. J.*, 2020, **7**(4), p 20–00152. <https://doi.org/10.1299/mej.20-00152>
30. T. Ohta, S. Tsutsumi, and N. Ma, Direct Measurement of Shot Velocity and Numerical Analysis of Residual Stress from Pneumatic Shot Peening, *Surf. Interfaces*, 2021, **22**, p 100827. <https://doi.org/10.1016/j.surfint.2020.100827>
31. K. Ogawa, T. Asano, A. Saito, A. Kawamura, M. Ogino, and H. Aihara, Measurement and Analysis of Shot Velocity in Pneumatic Shot Peening, *Trans. Jpn. Soc. Mech. Eng. Ser. C*, 1994, **60**, p 1120–1125. <https://doi.org/10.1299/kikaic.60.1120>
32. K. Nanbu, K. Itou, and N. Egami, Numerical Calculation of Particles Velocity under the Compressible Fluid in Fine Particle Bombardments, *Trans. Jpn. Soc. Mech. Eng. Ser. C*, 2010, **76**, p 3728–3735. <https://doi.org/10.1299/kikaic.76.3728>
33. T. Ohta and N. Ma, Shot Velocity Measurement using Particle Image Velocimetry and a Numerical Analysis of the Residual Stress in Fine Particle Shot Peening, *J. Manuf. Process.*, 2020, **58**, p 1138–1149. <https://doi.org/10.1016/j.jmapro.2020.08.059>
34. C. Wang, W. Li, J. Jiang, X. Chao, W. Zeng, and J. Yang, A New Methodology to Establish the Relationship Between Equivalent Shot Velocity and Air Pressure by Surface Roughness for Shot Peening, *Int. J. Adv. Manuf. Technol.*, 2021, **112**(7), p 2233–2247. <https://doi.org/10.1007/s00170-020-06423-2>
35. K. Tanaka, The cos α Method for x-ray Residual Stress Measurement using Two-dimensional Detector, *Mech. Eng. Rev.*, 2019, **6**(1), p 18–00378. <https://doi.org/10.1299/mer.18-00378>
36. M.G. Moore and W.P. Evans, Mathematical Correction for Stress in Removed Layers in x-ray Diffraction Residual Stress Analysis, *SAE Trans.*, 1958, **66**, p 6340–6345. <https://doi.org/10.4271/580035>
37. T. Ohta and Y. Sato, Numerical Analysis of Peen Forming for High-strength Aluminum Alloy Plates, *Mater. Trans.*, 2021, **62**(6), p 846–855. <https://doi.org/10.2320/matertrans.P-M2021818>
38. T. Ohta and Y. Sato, Effect of Saturation Peening on Shape and Residual Stress Distribution After Peen Forming, *Int. J. Adv. Manuf. Technol.*, 2022, **119**(7–8), p 4659–4675. <https://doi.org/10.1007/s00170-021-08473-6>
39. K. Mori, K. Osakada, and N. Matsuoka, Finite Element Analysis of Peening Process with Plasticity Deforming Shot, *J. Mater. Process. Technol.*, 1994, **45**(1–4), p 607–612. [https://doi.org/10.1016/0924-0136\(94\)90406-5](https://doi.org/10.1016/0924-0136(94)90406-5)

Publisher's Note Springer Nature remains neutral with regard to jurisdictional claims in published maps and institutional affiliations.

Springer Nature or its licensor (e.g. a society or other partner) holds exclusive rights to this article under a publishing agreement with the author(s) or other rightsholder(s); author self-archiving of the accepted manuscript version of this article is solely governed by the terms of such publishing agreement and applicable law.